FUDMA Journal of Renewable and Atomic Energy (FJoRAE)

ISSN: 3027-2335
Vol. 3 (1), June 2026, Pp 65-72
DOI: https://doi.org/10.33003/fjorae.2026.0301.89

Structural Properties of Manganese-Doped Zinc Selenide Nanoparticles Synthesized by High-Energy Ball Milling: An X-ray Diffraction and Raman Spectroscopic Study

***Ibrahim Muhammad Bagudo, Abdulrazaq Jimoh and Shamsuddeen Sani Alhassan**

Department of Physics, Faculty of Natural and Applied Sciences, Umaru Musa Yar'adua University, Katsina, Nigeria

*Corresponding Author's e-mail: ibrahim.bagudo@umyu.edu.ng

ABSTRACT

The structural properties of manganese-doped zinc selenide (ZnSe:Mn) nanoparticles, with an average particle size of approximately 3.5 nm, were investigated using X-ray diffraction (XRD) and Raman spectroscopy. Samples were synthesized by high-energy ball milling for 15, 30, and 40 h, with Mn content kept at 0.3%. XRD analysis identified three coexisting mineral phases–stilleite (ZnSe), selenium (Se), and zincite (ZnO)–and confirmed a cubic zincblende structure for stilleite alongside hexagonal structures for selenium and zincite, consistent with Joint Committee on Powder Diffraction Standards (JCPDS) reference data. Crystallite sizes, calculated using the Debye–Scherrer equation, decreased with increasing milling time, ranging from 34.8 Å to 29.4 Å, indicating progressive lattice refinement during milling. Raman spectra, recorded using a 514 nm excitation laser (0.75 mW), revealed dominant vibrational bands at 416, 866, 1782, and 2874 cm^{-1}, attributable to Mn-related lattice modes. The combined XRD and Raman results confirm successful incorporation of Mn into the ZnSe lattice and demonstrate that high-energy ball milling is a viable, low-cost route for producing nanostructured diluted magnetic semiconductors with tunable structural properties.

Keywords: Diluted magnetic semiconductor, ZnSe:Mn nanoparticles, High-energy ball milling, X-ray diffraction, Raman spectroscopy, Crystallite size

1.0 INTRODUCTION

Diluted magnetic semiconductors (DMSs), formed by doping conventional semiconductors with transition-metal ions, have attracted sustained research interest because of their combined semiconducting and magnetic properties. The strong sp–d exchange interaction between band electrons and the magnetic ions in DMSs underlies their distinctive magneto-optical behaviour and makes them promising candidates for spintronic devices, in which both charge and spin degrees of freedom can be exploited (Bhardwaj et al., 2025). Zinc selenide (ZnSe), an important wide-gap II–VI semiconductor, is a particularly attractive host material owing to its applications in solar cells, light-emitting devices, photodetectors as well as in photocatalytic and biological uses especially the doped versions (Sridevi et al., 2022; Teng et al., 2018; Lin et al., 2018; Yadav & Yaggi, 2015; Feng et al., 2014).

Manganese is among the most widely studied dopants for ZnSe because of the high fluorescence efficiency and magnetic ordering it imparts to the host lattice. ZnSe doped with Mn and other transition metals (V, Cr, Fe, Co, Ni) has been reported to exhibit ferromagnetism, although the microscopic origin of this behaviour remains incompletely understood (Kumar et al., 2023). It has been proposed that ferromagnetism in such systems can be induced by nanoscale inclusions of transition-metal oxides or by clusters enriched in

magnetic ions, motivating systematic structural characterization of Mn-doped ZnSe nanoparticles.

Several synthesis routes for ZnSe:Mn nanostructures have been reported, including hydrothermal and photocatalytic-grade nanoparticle synthesis (Sridevi et al., 2022; Qiao et al., 2019) and Mn-doped oxide nanostructures produced for related optoelectronic applications (Vrithias et al., 2023), as well as mechanochemical solid-state milling routes for nanocrystalline and nanocomposite materials more broadly (El-Eskandarany et al., 2021). Among the reported methods of synthesizing nanostructures, high-energy ball milling offers a simple and low-cost approach capable of producing high-quality nanomaterials without the need for high synthesis temperatures (El-Eskandarany, 2020).

However, comparatively few studies have systematically tracked how milling duration influences the coexisting mineral phases, lattice parameters, and crystallite size of ZnSe:Mn produced by high-energy ball milling. The present study addresses this gap by synthesizing Mn-doped ZnSe nanoparticles via high-energy ball milling at three milling durations (15, 30, and 40 h) and characterizing the resulting structural evolution using X-ray diffraction and Raman spectroscopy. The specific objective is to determine the structural behaviour of ZnSe:Mn–including phase composition, lattice parameters, and crystallite size–as a function of milling time.

2.0 MATERIALS AND METHOD

2.1 Sample Preparation by High-Energy Ball Milling

Mn-doped ZnSe (nominal composition $Mn_{0.3}Zn_{0.7}Se$) was synthesized mechanochemically following high-energy ball milling procedures consistent with authors' previous report (Muh'd et al., 2015). Elemental Zn, Se, and Mn powders of 99.9% purity were thoroughly mixed and sealed under argon atmosphere in a stainless-steel grinding jar together with 3 mm diameter steel balls. Milling was carried out in a Retsch PM100 planetary ball mill at a ball-to-powder mass ratio of 10:1 and a rotation speed of 500 rpm for durations of 15, 30, and 45 h. Small quantities of powder were withdrawn from the jar at each milling interval for subsequent structural characterization.

2.2 X-ray Diffraction

Microstructural characterization was performed using a PANalytical X'Pert PRO X-ray diffractometer with Cu Kα radiation (λ = 1.54056 Å), scanning over a diffraction angle (2θ) range of 24^0–770^0. Crystallite sizes were estimated from the diffraction peak broadening using the Debye–Scherrer equation:

$$D = \frac{K\lambda}{(B\cos\theta)} \quad (1)$$

where D is the crystallite size, K is the shape factor (0.89–0.9), λ is the X-ray wavelength, B is the full width at half maximum of the diffraction peak (in radians), and θ is the Bragg angle.

2.3 Raman Spectroscopy

Raman spectra were collected at room temperature using a Jasco FP-8300 spectrofluorometer-based Raman system with 514 nm laser excitation at 0.75 mW power. For each milling duration (15, 30, and 40 h), spectra were recorded over the range 100–3000 cm^{-1} at several distinct points on the sample to assess spectral reproducibility.

3.0 RESULTS AND DISCUSSION

X-ray diffraction analysis was used to track the structural evolution of the ZnSe:Mn samples milled for 15, 30, and 40 h, while Raman spectroscopy was used to probe the corresponding vibrational property.

3.1 Phase Identification by XRD

Diffractograms of ZnSe:Mn milled for 15, 30, and 40 h displayed well-defined, sharp diffraction peaks indicative of good crystallinity as depicted in Figure 1.

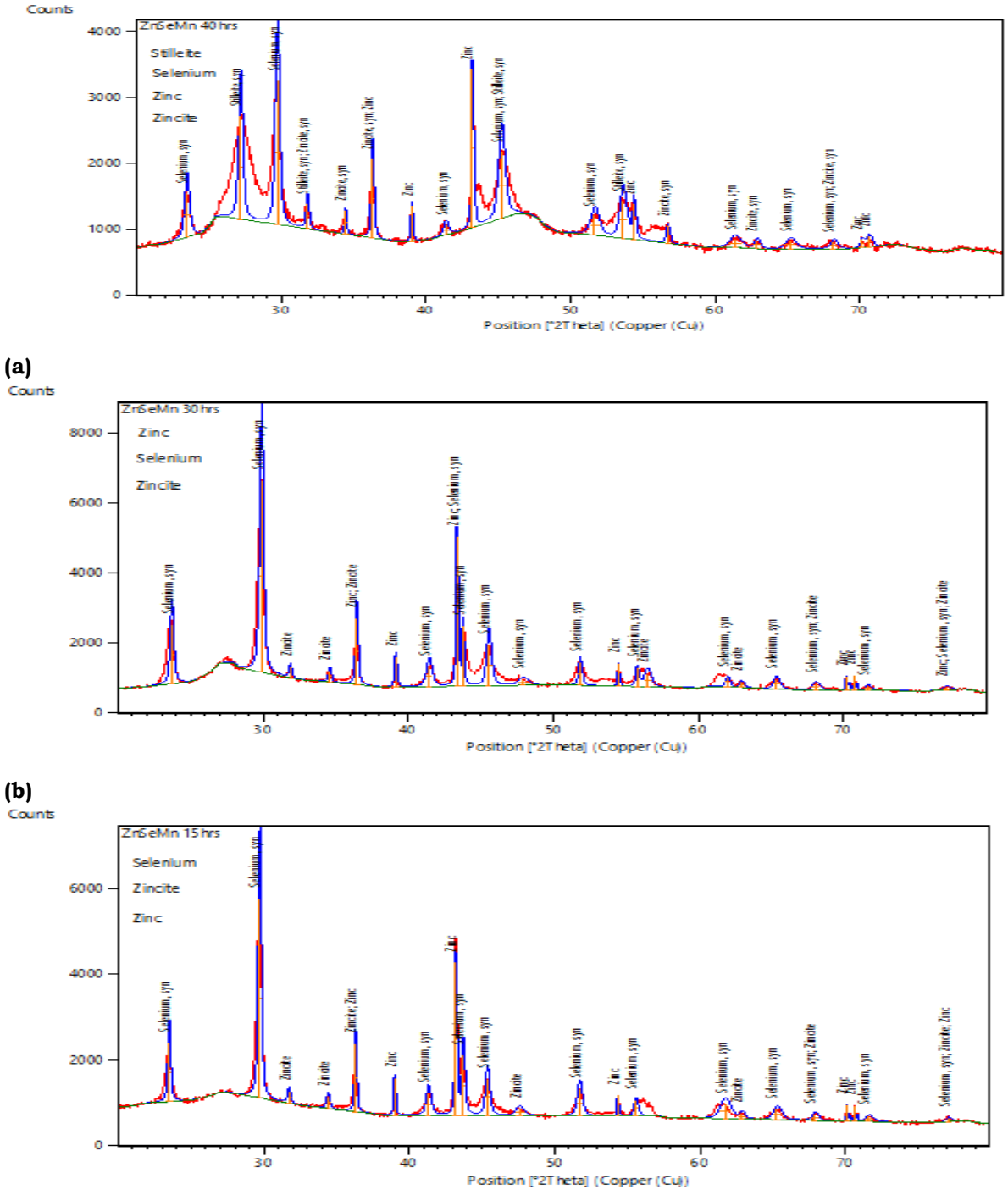

Figure 1: Diffraction patterns of ZnSe:Mn for: (a) 40 h (b) 30 h (c) 15 h. The blue, red and orange colors represent selenium, stilleite and zincite respectively.

Three coexisting mineral phases were identified across the samples: stilleite (ZnSe), selenium (Se), and zincite (ZnO). The selenium and zincite phases reflect the structural and crystalline character of the milled powders, while the stilleite phase is associated with both the structural and magnetic behaviour of the Mn-doped material. Table 1 summarizes the principal diffraction angles (2θ) used to distinguish each phase at the three milling times.

Table 1: Distinguishing XRD peaks for the stilleite, zincite, and selenium phases at each milling time

Milling time	Stilleite (ZnSe) peaks (2θ)	Zincite (ZnO) peaks (2θ)	Selenium (Se) peaks (2θ)
40 h	27°, 31°, 45°, 54°	32°, 34°, 36°, 57°, 63°, 68°	24°, 30°, 45°, 52°, 65°, 68°
30 h	Not observed	32°, 35°, 36°, 56°, 63°, 77°	24°, 30°, 41°, 44°, 46°, 48°, 52°, 56°, 62°, 63°, 70°, 77°
15 h	Not observed	32°, 34°, 36°, 48°, 63°, 69°, 77°	24°, 30°, 41°, 44°, 45°, 48°, 54°, 63°, 65°, 68°, 72°, 77°

The stilleite phase was detected only in the sample milled for 40 h, suggesting that longer milling promotes the formation or crystallization of the ZnSe:Mn phase, whereas the zincite and selenium phases were present at all three milling durations, consistent with partial oxidation and elemental Se retention during processing.

3.2 Crystallographic Parameters

Lattice parameters (a=b=c), unit-cell volume, and X-ray density obtained from the diffractograms are compared with corresponding JCPDS reference values in Tables 2 and 3. The obtained lattice parameters confirm a cubic zincblende structure for the stilleite phase, while the selenium and zincite phases exhibit hexagonal structures, in agreement with previously reported crystallite-size and lattice-parameter determinations for high-energy-milled nanomanganite systems (Manh et al., 2023). All samples showed good agreement with the JCPDS reference cards (01-088-2345 for stilleite, 01-073-0456 for selenium, and 96-900-4181 for zincite).

Table 2: Crystallographic parameters of ZnSe:Mn milled for 30 and 40 h, compared with JCPDS reference data

Parameter	Stilleite (JCPDS)	Stilleite (this work)	Selenium (this work)	Selenium (JCPDS)	Zincite (this work)	Zincite (JCPDS)
a = b = c (Å)	5.6511	5.6700	4.3662	4.3563	3.2490	3.149
Unit cell volume (Å³)	182.18	182.28	81.78	80.54	47.60	46.63
X-ray density (g/cm³)	5.26	5.26	4.81	3.51	5.68	4.86

Table 3: Crystallographic parameters of ZnSe:Mn milled for 15 h, compared with JCPDS reference data

Parameter	Stilleite (JCPDS)	Stilleite (this work)	Selenium (this work)	Selenium (JCPDS)	Zincite (this work)	Zincite (JCPDS)
a = b = c (Å)	1.8810	2.6650	4.3662	4.3563	3.2530	3.149
Unit cell volume (Å³)	29.80	30.43	81.78	80.54	47.72	46.63
X-ray density (g/cm³)	7.10	7.14	4.81	3.51	5.66	4.86

3.3 Crystallite Size Analysis

The (hkl) reflections, d-spacings, peak widths, and corresponding crystallite sizes for the stilleite, selenium, and zincite phases, calculated using the equation (1), are presented in Tables 4–6. Crystallite sizes for the stilleite phase ranged from approximately 3.05 Å to 4.19 Å across the (111) to (511) reflections, with the smallest sizes associated with the lowest-angle, most intense (111) reflection.

Table 4: XRD reflection data and crystallite size for the stilleite (ZnSe) phase

(h k l)	d-spacing (Å)	Peak width (°2θ)	Peak intensity (counts/s)	Crystallite size (Å)
111	3.27358	27.220	100.0	3.0524
200	2.83500	31.532	0.4	3.0826
220	2.00465	45.195	58.6	3.2134
311	1.70957	53.562	31.7	3.3231
222	1.63679	56.149	0.1	3.3623
400	1.41750	65.834	7.0	3.5340
331	1.30079	72.624	9.4	3.6816
420	1.26785	74.827	0.1	3.7351
422	1.15738	83.450	11.0	3.9749
511	1.09119	89.809	5.6	4.1885

Table 5: XRD reflection data and crystallite size for the selenium phase

(h k l)	d-spacing (Å)	Peak width (°2θ)	Peak intensity (counts/s)	Crystallite size (Å)
100	3.78124	23.509	49.1	3.0048
101	3.00565	29.699	100.0	3.0718
110	2.18310	41.323	14.62	3.1143
012	2.07189	43.652	24.3	3.1288
111	1.99770	45.361	18.6	3.1890
200	1.89062	48.087	2.3	3.2366
201	1.76634	51.711	15.5	3.3287
003	1.65120	55.616	3.3	3.3746
112	1.63773	56.114	7.2	3.4703
103	1.51321	61.201	2.5	3.5318
022	1.50282	61.670	6.7	3.6420
210	1.42917	65.229	9.4	3.7134
121	1.37317	68.245	3.0	3.7381
113	1.31693	71.595	2.3	3.8421
300	1.26041	75.345	0.1	3.9261
023	1.24366	76.542	0.5	3.8700
212	1.23788	76.965	1.6	4.0792
031	1.22149	78.192	2.9	4.1802
104	1.17689	81.767	1.2	4.1734
302	1.12333	86.586	1.7	4.0174
221	1.09155	89.771	0.4	4.1755

Table 6: XRD reflection data and crystallite size for the zincsite (ZnO) phase

(h k l)	d-spacing (Å)	Peak width (°2θ)	Peak intensity (counts/s)	Crystallite size (Å)
100	2.81372	31.777	50.7	3.0048
002	2.60350	34.420	29.4	3.0718
101	2.47542	36.261	100.0	3.1143
102	1.91095	47.544	14.9	3.1288
110	1.62450	56.612	25.8	3.1890
103	1.47722	62.859	24.9	3.2366
200	1.40686	66.396	3.3	3.3287
112	1.37821	67.961	14.8	3.3746
201	1.35816	69.105	9.4	3.4703

004	1.30175	72.561	1.6	3.5318
202	1.23771	76.977	2.2	3.6420
104	1.18144	81.385	1.5	3.7134
203	1.09292	89.628	5.7	3.7381

The crystallite size of the ZnSe:Mn nanoparticles decreased with increasing Mn content/milling time, from 34.8 Å to 29.4 Å, indicating that extended milling promotes progressive grain refinement, consistent with the expected mechanism of repeated fracturing and cold welding during high-energy ball milling

3.4 Raman Spectroscopy

Raman spectra recorded for the 15, 30, and 40 h milled samples using 514 nm laser excitation (0.75 mW) showed peak displacements within the 100–3000 cm^{-1} range (Figure 2).

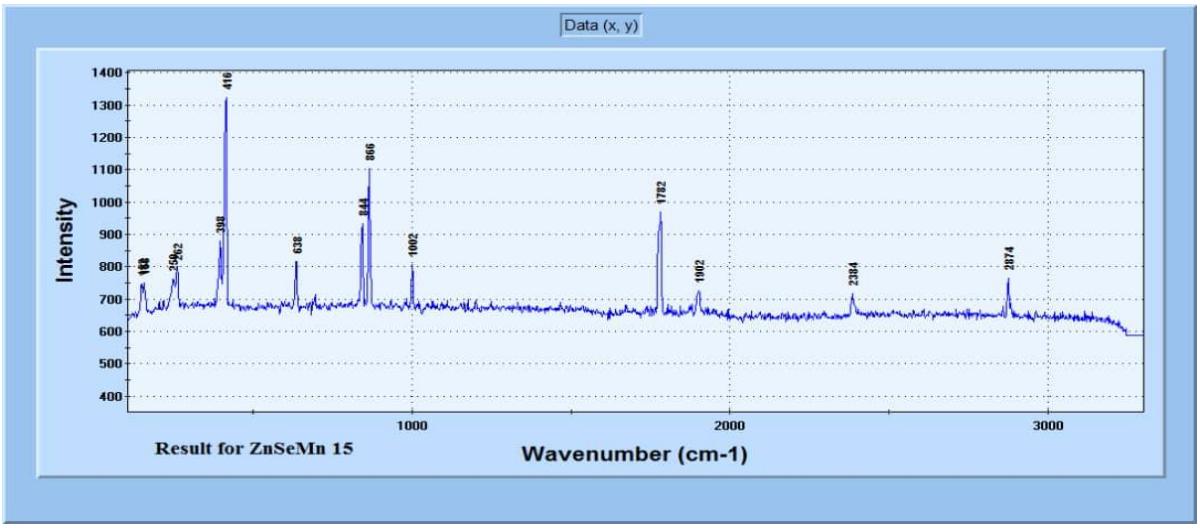

(a)

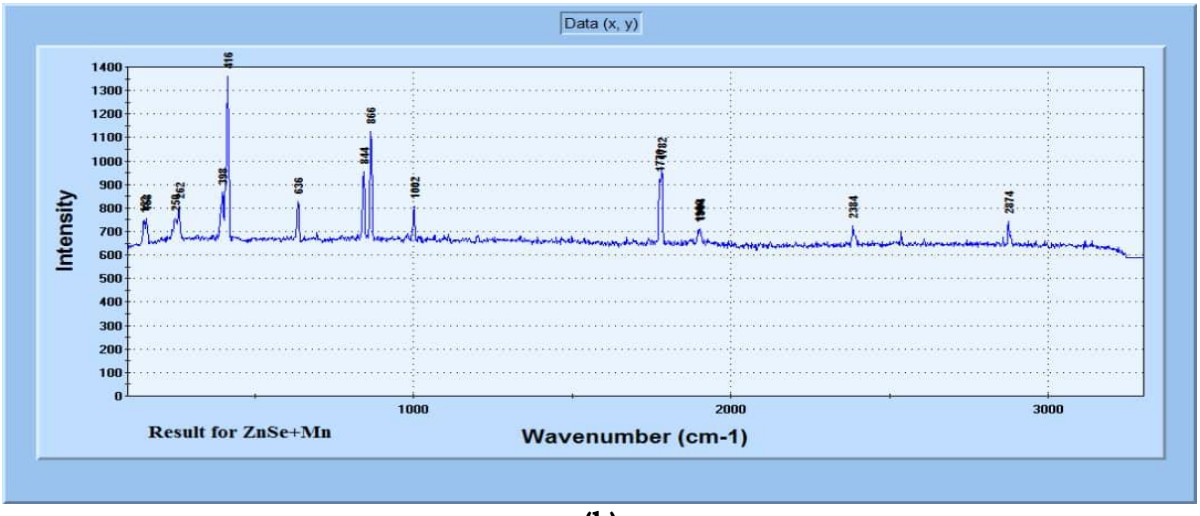

(b)

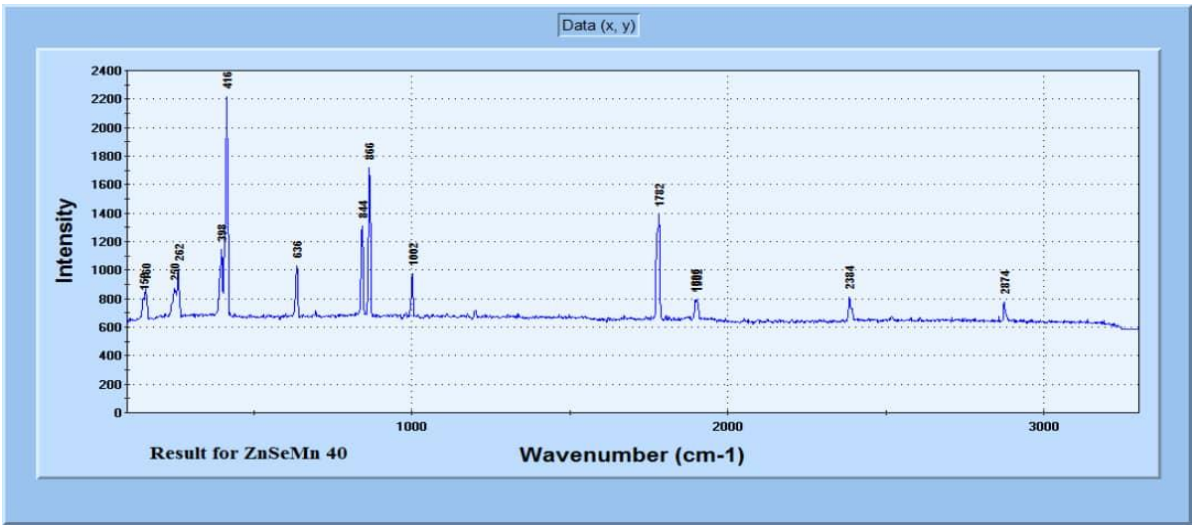

(c)

Figure 2: Raman spectra of ZnSe:Mn for: (a) 15 h (b) 30 h (c) 40 h

The dominant vibrational bands were observed at 416, 866, 1782, and 2874 cm^{-1}. Because diluted magnetic semiconductors typically exhibit weak Raman scattering, particularly at low laser powers, care was taken to avoid laser-induced phase transformations during data collection. The persistence of these bands across all three milling times suggests that the local vibrational environment of the ZnSe:Mn lattice is preserved despite progressive crystallite refinement, while subtle intensity variations are consistent with the changing phase composition (stilleite, selenium, zincite) identified by XRD.

4.0 CONCLUSION

Mn-doped ZnSe nanoparticles were successfully synthesized by high-energy ball milling at 15, 30, and 40 h, and their structural properties were characterized by XRD and Raman spectroscopy. XRD analysis identified three coexisting phases – stilleite, selenium, and zincite – with the stilleite (ZnSe) phase, which carries the dopant-related magnetic character, becoming detectable only after extended milling (40 h). The stilleite phase exhibits a cubic zincblende structure, while selenium and zincite display hexagonal structures, both in good agreement with JCPDS reference data. Crystallite size decreased with increasing milling time, from 34.8 Å to 29.4 Å, reflecting progressive grain refinement. Raman spectroscopy confirmed characteristic Mn-related vibrational bands at 416, 866, 1782, and 2874 cm^{-1}, consistent with successful Mn incorporation into the ZnSe host lattice. These findings support high-energy ball milling as a simple, low-cost, and scalable route for producing structurally tunable ZnSe:Mn nanoparticles for spintronic and optoelectronic applications. Further work using complementary techniques such as SQUID magnetometry is recommended to directly probe the magnetic behaviour of the synthesized diluted magnetic semiconductor.

REFERENCES

Bhardwaj, P., Singh, J., Verma, V., & Kumar, R. (2025). Harnessing the duality of magnetism and conductivity: A review of oxide-based dilute magnetic semiconductors. Physica B: Condensed Matter, 696, Article 416596. https://doi.org/10.1016/j.physb.2024.416596

El-Eskandarany, M. S., Al-Hazza, A., Al-Hajji, L. A., Ali, N., Al-Duweesh, A. A., Banyan, M., & Al-Ajmi, F. (2021). Mechanical milling: A superior nanotechnological tool for fabrication of nanocrystalline and nanocomposite materials. Nanomaterials, 11(10), 2484. https://doi.org/10.3390/nano11102484

El-Eskandarany, M.S. (2020). Mechanical Alloying: Energy, Surface Protective Coating and Medical Applications, 3rd ed.; Elsevier: Oxford, UK.

Feng, B.; Cao, J., Yang, J., Yang, S. & Han, D.(2014). Characterization and photocatalytic activity of ZnSe nanoparticles synthesized by a facile solvothermal method, and the effects of different solvents on these properties. Material Research Bulletin, 60, 794–801.

Kumar, S., Ahmed, F., Shaalan, N. M., Arshi, N., Dalela, S., & Chae, K. H. (2023). Structural, optical, magnetic and electrochemical properties of CeXO2 (X: Fe, and Mn) nanoparticles. Materials, 16(6), 2290. https://doi.org/10.3390/ma16062290

Lin, M.-H., Parasuraman, P. S. & Ho, C.-H. (2018). The study of near-band-edge property in oxygen-incorporated ZnS for acting as an efficient crystal photocatalyst. ACS Omega, 3, 6351−6359.

Manh, D. H., Nha, T. T. N., Phong, L. T. H., Nam,P. H., Thanh, T. D., & Phong.P. T. (2023). Determination of the crystalline size of hexagonal La1−xSrxMnO3 (x = 0.3) nanoparticles from X-ray diffraction - a comparative study. RSC Advances, 13, 25007-25017. https://doi.org/10.1039/D3RA04018F

Muh'd, I.B., Talib, Z.A., Zainal, Z. Chyi J, Mofdal M. (2015). Mechanochemical solid state synthesis and optical properties of $Cd_{0.5}Zn_{0.5}Se$ nanocrystals. Journal of Material Sciences, 50, 457–462. https://doi.org/10.1007/s10853-014-8605-5

Qiao, F., Kang, R., Liang, Q., Cai, Y., Bian, J. & Hou, X. (2019). Tunability in the optical and electronic properties of ZnSe microspheres via Ag and Mn doping. ACS Omega, 4, 12271-12277.

Sridevi, D. V., Vadivel, R., Perumal, S., Sundaravadivel, E., & Sivaramakrishnan, V. (2022). A facile synthesis of Mn-doped ZnSe nanoparticles for an enhanced photocatalytic activity and biological applications. Ceramics International, 48(19), 29394-29402. https://doi.org/10.1016/j.ceramint.2022.06.050

Teng, F., Hu, K., Ouyang, W. & Fang, X. (2018). Photoelectric Detectors Based on Inorganic p-Type Semiconductor Materials. Advanced Materials, 30, 1706262.

Vrithias, N. R., Katsara, K., Papoutsakis, L., Papadakis, V. M., Viskadourakis, Z., Remediakis, I. N., & Kenanakis, G. (2023). Three-dimensional-printed photocatalytic sponges decorated with Mn-doped ZnO nanoparticles. Materials, 16(16), 5672. https://doi.org/10.3390/ma16165672

Yadav, K. & Jaggi, N. (2015). Effect of Ag doping on structural and optical properties of ZnSe nanophosphors. Material Science Semiconductor Proceedings, 30, 376−380.